Radial viscous fingering in yield stress fluids: Onset of pattern formation

João V. Fontana, Sérgio A. Lira, and José A. Miranda*
Departamento de Física, Universidade Federal de Pernambuco, Recife, PE 50670-901, Brazil
(Received 14 September 2012; published 18 January 2013)

We report analytical results for the development of interfacial instabilities in a radial Hele-Shaw cell in which a yield stress fluid is pushed by a Newtonian fluid of negligible viscosity. By dealing with a gap averaging of the Navier-Stokes equation, we derive a Darcy-law-like equation for the problem, valid in the regime of high viscosity compared to yield stress effects. A mode-coupling approach is executed to examine the morphological features of the fluid-fluid interface at the onset of nonlinearity. Within this context, mechanisms for explaining the rising of tip-splitting and side-branching events are proposed.

DOI: 10.1103/PhysRevE.87.013016 PACS number(s): 47.15.gp, 47.54.Bd, 47.50.Gj

I. INTRODUCTION

It is well known that when a less viscous fluid pushes a more viscous one in the confined geometry of a Hele-Shaw cell, the interface separating the fluids develops the Saffman-Taylor instability [1] leading to the formation of fingerlike patterns [2]. The specific morphology of these patterns depend on the nature of the fluids, and on the geometry of the flow. Most of the existing studies on the viscous fingering instability refer to Newtonian fluids. In this case, the resulting interfacial shapes range from a single, smooth, steady-state finger in rectangular (or, channel) geometry [3–11], to multifingered structures in which repeated tip splitting produces highly ramified patterns in the radial flow setup [12–23]. These pattern forming phenomena have been extensively studied during the last 50 years through analytical calculations, numerical simulations, and experiments.

Although not as numerous as in the Newtonian fluid case, other Hele-Shaw flow investigations have revealed that a distinct variety of patterns can be formed when one of the fluids is non-Newtonian [24]. While Newtonian fluids are characterized by a constant viscosity, non-Newtonian fluids display a multiplicity of hydrodynamic behaviors ranging from elasticity and plasticity to shear thinning and shear thickening, and in general have a shear-dependent viscosity.

The rheological properties of non-Newtonian fluids exert a profound effect on the shape of the emerging interfacial patterns in Hele-Shaw flows. Rectangular and radial Hele-Shaw experiments involving non-Newtonian fluids like polymer solutions, liquid crystals, clays and foams unveiled pattern morphologies presenting snowflake-like shapes [25] and fracturelike structures [26,27]. For shear-thinning fluids traditional finger tip-splitting events are inhibited, and the appearance of dendritic patterns with side branching is favored. Cracklike patterns presenting angular branches and sharp tips have also been found. On the other hand, flow with shear-thickening fluids [28] displays patterns similar to those found in Newtonian fluids but with either narrowing or widening of the fingers, which can present asymmetric humps. This morphological diversity and rich dynamical behavior motivated a number of theoretical studies of the problem through linear and weakly nonlinear analyzes, and sophisticated numerical simulations [29–38].

Despite all the efforts and important results obtained by researchers on the development of viscous fingering in non-Newtonian Hele-Shaw flows, the pattern forming dynamics with yield stress fluids has been relatively underlooked. In contrast to Newtonian fluids, yield stress fluids [39,40] can support shear stresses without flowing. As long as the stress remains below to a certain critical value they do not flow, but respond elastically to deformation. So such materials possess properties of both viscous fluids and elastic solids, behaving like a "semisolid." On the theoretical side, a linear stability analysis of the Saffman-Taylor problem in rectangular and radial cells with yield stress fluids [41] has predicted that the instability can be drastically modified. On the experimental arena some interesting findings have been disclosed in channel geometry [42,43]: depending on whether viscous effects or yield stresses dominates, fractal patterns, or ramified structures where multiple fingers propagate in parallel may arise.

In a more recent experimental work [44] fingering in a yield stress fluid in rectangular as well as in radial Hele-Shaw cells has been examined. As in Ref. [42,43] different regimes, leading to diverse pattern morphologies have been observed: At low velocities (where yield stress dominates) ramified structures arise; however, for higher velocities (viscous effects prevail), in addition to tip splitting, interesting side-branching instabilities become apparent. Although the behavior at the low velocity regime can be quantitatively explained from the linear stability results presented in Ref. [41], the nonlinear side-branching and tip-splitting instabilities detected at higher velocities are not fully understood to date. So, a theoretical study addressing these suggestive pattern forming phenomena in yield stress fluids is still lacking.

In this work we carry out the analytical weakly nonlinear analysis of the problem in which a yield stress fluid flows in a radial Hele-Shaw cell. We focus on the regime in which viscosity effects are prevalent over yield stress. By exploring the onset of nonlinear effects we try to gain analytical insight into the dynamic process of fingering formation. In particular, we seek to understand how mode-coupling dynamics leads to basic morphological features and behaviors observed experimentally in such non-Newtonian Hele-Shaw flows [44].

The article is organized as follows: Sec. II formulates the problem and derives a generalized Darcy-like law. In Sec. III

*jme@df.ufpe.br

we perform a Fourier decomposition of the interface shape, and from the alternative form of Darcy's law study the influence of weak yield stress effects on the development of interfacial patterns. Coupled, nonlinear, ordinary differential equations governing the time evolution of Fourier amplitudes are derived in detail. Section IV discusses both linear and weakly nonlinear dynamics. It concentrates on the dawning of finger tip-splitting and side-branching phenomena. Our main conclusions are summarized in Sec. V.

II. PROBLEM FORMULATION AND DARCY'S LAW APPROACH

The Hele-Shaw cell is depicted in Fig. 1 and consists of two parallel plates separated by a small distance b. Consider the displacement of a non-Newtonian fluid of viscosity η and yield stress σ_0, by a Newtonian fluid of negligible viscosity in such confined geometry. The surface tension between the fluids is denoted by γ. The Newtonian fluid is injected at a constant areal flow rate Q at the center of the cell, along the direction perpendicular to the plates (z axis).

We focus on deriving the relevant hydrodynamic equation for a Hele-Shaw flow of a yield stress fluid. Our main goal is to obtain a Darcy's like law which relates the gap-averaged velocity with the pressure gradient and the yield stress, taking into account the coupling between them. We start by taking the Navier-Stokes equation for an incompressible viscous fluid [45]

$$\rho\left[\frac{\partial \mathbf{u}}{\partial t}+(\mathbf{u}\cdot\nabla)\mathbf{u}\right]=-\nabla P-\nabla\cdot\boldsymbol{\tau}, \tag{1}$$

where ρ is density, $\mathbf{u}$ denotes the three-dimensional velocity, P is the pressure, and $\boldsymbol{\tau}$ represents the stress tensor that includes the yield stress. In the scope of the lubrication approximation, where the distance between the plates b is much smaller than the unperturbed radius R of the fluid-fluid interface, the motion is a creeping flow. Therefore, we may neglect the inertial terms between square brackets in Eq. (1), as well as impose that the prevailing terms in $\nabla\cdot\boldsymbol{\tau}$ are those with transversal derivatives. Within this framework, we also consider that pressure is constant along the transversal direction (z axis). Thus, by integrating (1) we obtain

$$\tau_{iz}=\left|\frac{b}{2}-z\right|\nabla_i P, \tag{2}$$

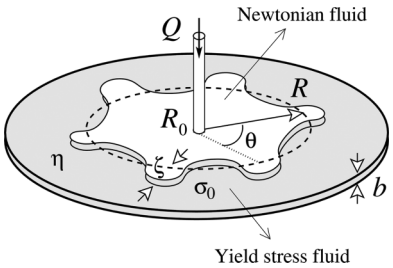

FIG. 1. Schematic configuration of radial flow in a Hele-Shaw cell. The inner fluid is Newtonian and has negligible viscosity. The outer fluid is a yield stress fluid. The unperturbed fluid-fluid interface (dashed curve) is a circle of radius R. All physical parameters are defined in the text.

where $i=r,\theta$ is the label that indicates polar radial or azimuthal components, with the origin placed at the center of the droplet. We have used the symmetry of the flow to state that the shear stress is zero at the midplane $z=b/2$ (since the plates are located at $z=0$ and $z=b$).

Furthermore, as a constitutive relation for yield stress fluids, we use the Bingham model [24]. It states that, for a given shear stress higher than the fluid yield stress magnitude σ_0, there is flow and the stress tensor is given by

$$\tau_{iz}=-\left[\eta\frac{\partial u_i}{\partial z}+\sigma_i\right]. \tag{3}$$

This situation corresponds to $|\boldsymbol{\tau}|>\sigma_0$, where $|\boldsymbol{\tau}|=\sqrt{\tau_{rz}^2+\tau_{\theta z}^2}$. We point out that, in contrast to previous works [46–49], here we allow the yield stress to exhibit both r and θ polar components, in such a way that its response is now opposite to the stress tension. This is precisely what will allow us to couple the yield stress to the velocity direction by the end of our derivation. From Eq. (2) we see that the stress tension is parallel to pressure gradient and we may write $\sigma_i=-\sigma_0\nabla_i P/|\nabla P|$.

On the other hand, if $|\boldsymbol{\tau}|\leqslant\sigma_0$, the shear stress do not overcome the yield stress, thus there is no flow

$$\frac{\partial u_i}{\partial z}=0, \tag{4}$$

meaning that $\sigma_i=-\tau_{iz}$.

Since the problem is symmetric with respect to the midplane $z=b/2$, we may assume $0\leqslant z\leqslant b/2$ for simplicity. From Eq. (2) we find the critical height z_c which separates the sheared region from the unsheared region

$$z_c=\frac{b}{2}-\frac{\sigma_0}{|\nabla P|}. \tag{5}$$

Then, by using Eq. (2) and the profile velocity continuity at $z=z_c$, it is possible to determine the velocity profile for both regions

$$\begin{aligned}\mathbf{u}&=-\frac{\nabla P}{\eta}\left[z\left(z_c-\frac{z}{2}\right)\right]\quad\text{for}\quad 0\leqslant z<z_c,\\ \mathbf{u}&=-\frac{\nabla P}{\eta}\frac{z_c^2}{2}\quad\text{for}\quad z_c\leqslant z\leqslant\frac{b}{2}.\end{aligned} \tag{6}$$

It is well known that this velocity profile cannot be exact for different kind of flows [50–52]. However, the expression given by Eq. (6) is a good approximation when one only seeks the relationship between the pressure drop and the mean velocity [41], which is exactly our case.

We define the gap-averaged velocity as

$$\mathbf{v}=\frac{1}{b}\int_0^b\mathbf{u}\,dz, \tag{7}$$

and by gap averaging (6) we finally obtain a dimensionless modified Darcy's law for yield stress fluids

$$\mathbf{v}=-\nabla P\left[1-\frac{\delta}{|\nabla P|}+\frac{4\delta^3}{27|\nabla P|^3}\right]. \tag{8}$$

The dimensionless parameter

$$\delta=\frac{\pi\sigma_0 b R_f}{2\eta Q} \tag{9}$$

is a modified plasticity number and quantifies the ratio between yield stress and viscous forces. Hereafter, we take δ as positive (since $Q > 0$) and refer to it as the yield stress parameter. We point out that in Eq. (8) lengths and velocities were rescaled by R_f and $Q/(2\pi R_f)$, respectively, where R_f is the radius of the unperturbed interface at $t = t_f$ [see Eq. (11)]. From this point on we use the dimensionless version of the equations. Our Eq. (8) is in agreement with the results of Ref. [46], which studied the simpler situation involving the purely radial flow of a perfectly circular droplet.

Since we are interested in examining the interface destabilization process, we consider the regime where viscous forces prevail over the yield stress and flow is facilitated, which corresponds to $\delta \ll 1$. Therefore, we may neglect the third-order term in δ shown in Eq. (8). Moreover, since (8) states that velocity is parallel to the pressure gradient, we may rewrite it in a more convenient way as

$$\nabla P = -\mathbf{v}\left[1 + \frac{\delta}{|\mathbf{v}|}\right]. \tag{10}$$

Equation (10) is an alternative form of Darcy's law ideally suited to describe the Hele-Shaw flow dynamics in the weak yield stress regime. The usual Newtonian Darcy's law is recovered when we set $\delta = 0$.

We close this section by calling the reader's attention to an important distinction between our current results and the ones obtained in Ref. [32]. Kondic *et al.* [32] studied a nonNewtonian model where shear-thinning fluids were analyzed. In their work, a theoretical model for a shear rate dependent viscosity results in generalized Darcy's law [their Eq. (2)], which is distinct from our Darcy's law [Eq. (10)] for yield stress fluids. It should be emphasized that we do not propose a shear-thinning model, i.e., a shear-dependent viscosity to a nonNewtonian fluid. Rather, we seek for a Darcy's law to a yield stress fluid, a nonNewtonian fluid that can support shear stresses without flowing, and derive a specific modified Darcy's law [our Eq. (10)] to describe flow of such a fluid in the confined geometry of a Hele-Shaw cell. Moreover, contrary to what is done in Ref. [32], our approach considers a Bingham model [Eq. (3)] where η denotes a Newtonian (constant) viscosity.

III. MODE-COUPLING EQUATION

To perform the weakly nonlinear analysis of the system, we consider that the initial circular fluid-fluid interface is slightly perturbed (see Fig. 1), $\mathcal{R} = R(t) + \zeta(\theta,t)$ ($\zeta/R \ll 1$), where the time dependent unperturbed radius is given by

$$R(t) = \sqrt{R_0^2 + 2t}, \tag{11}$$

R_0 being the dimensionless unperturbed radius at $t = 0$. The interface perturbation is written in the form of a Fourier expansion

$$\zeta(\theta,t) = \sum_{n=-\infty}^{+\infty} \zeta_n(t) \exp(in\theta), \tag{12}$$

where $\zeta_n(t) = (1/2\pi)\int_0^{2\pi} \zeta(\theta,t)\exp(-in\theta)\,d\theta$ denotes the complex Fourier mode amplitudes and n is an integer wave number. In our Fourier expansion (12) we include the $n = 0$ mode to keep the area of the perturbed shape independent of the perturbation ζ. Mass conservation imposes that the zeroth mode is written in terms of the other modes as $\zeta_0 = -(1/2R)\sum_{n\neq 0}|\zeta_n(t)|^2$. We stress that our perturbation scheme keeps terms up to the second order in ζ and up to first order in δ.

The weakly nonlinear approach to radial, Newtonian Hele-Shaw flow developed in Ref. [18], related the fluid velocity to a *scalar* velocity potential $\mathbf{v} = -\nabla\phi$, this replacement made possible by the irrotational nature of the flow for Newtonian fluids. For non-Newtonian fluids, in contrast, flows governed by the modified Darcy's law (10) exhibit vorticity. Hence, as in Ref. [36] we perform our calculations using a *vector* potential $\mathbf{v} = \nabla \times \mathbf{A}$. The most general form of the vector potential can be written as

$$\mathbf{A} = \left[\theta + \sum_{m,n\neq 0} A_{mn}\left(\frac{R}{r}\right)^m \exp(in\theta)\right]\hat{\mathbf{z}}, \tag{13}$$

where A_{mn} are the Fourier coefficients of the velocity vector potential and $\hat{\mathbf{z}}$ is the outward unit-normal to the upper cell plate. The radial and polar components of the fluids velocities are

$$v_r = \frac{1}{r} + \sum_{m,n\neq 0} inA_{mn}\left(\frac{R^m}{r^{m+1}}\right)\exp(in\theta) \tag{14}$$

and

$$v_\theta = \sum_{m,n\neq 0} mA_{mn}\left(\frac{R^m}{r^{m+1}}\right)\exp(in\theta). \tag{15}$$

We exploit the fact that ∇P must be curl free, and impose the so-called solvability condition $\nabla \times \nabla P = 0$. It simplifies the general form of the vector potential expansion given in Eq. (13). The solvability condition reveals that, without loss of generality, one can rewrite the vector potential as

$$\mathbf{A} = \left\{\theta + \sum_{n\neq 0} A_n\left(\frac{R}{r}\right)^{|n|}\exp(in\theta) + \delta\left[\sum_{n\neq 0} B_n\left(\frac{R}{r}\right)^{|n|} r\exp(in\theta)\right]\right\}\hat{\mathbf{z}}, \tag{16}$$

replacing the array of coefficients A_{mn} with the simpler set of A_n and B_n. Observe that the vector potential (16) is simply a superposition of a purely Newtonian term ($\propto \delta^0$, coefficients A_n) and a non-Newtonian contribution ($\propto \delta^1$, coefficients B_n)

$$\mathbf{A} = \mathbf{A}_N + \mathbf{A}_{NN}. \tag{17}$$

The flow described by $\mathbf{A}_N$ is irrotational, while $\mathbf{A}_{NN}$ has a curl.

Similarly, we express the pressure of the outer fluid as a sum of Newtonian and non-Newtonian pressures, and propose a general form for their Fourier expansion

$$P = P_N + P_{NN}, \tag{18}$$

where

$$P_N = -\log\left(\frac{r}{R}\right) + \sum_{n\neq 0} p_n\left(\frac{R}{r}\right)^{|n|}\exp(in\theta) \tag{19}$$

and

$$P_{NN} = \delta\left[-r + \sum_{n\neq 0} q_n \left(\frac{R}{r}\right)^{|n|} r\exp(in\theta)\right]. \tag{20}$$

The gradient of the complex pressure field (18) must satisfy the non-Newtonian Darcy's law given by Eq. (10). By inspecting the r and θ components of Eq. (10), and by examining the Newtonian and non-Newtonian components of it, we can express the Fourier coefficients of P_N, P_{NN}, and $\mathbf{A}_{NN}$ in terms of the Fourier coefficients of $\mathbf{A}_N$,

$$p_n = i\,\mathrm{sgn}(n)(A_n), \tag{21}$$

$$q_n = iA_n\mathrm{sgn}(n)\beta(n) + \sum_{m\neq 0, m\neq n} mA_m(n-m)A_{n-m}k(n,m), \tag{22}$$

$$B_n = A_n\alpha(n) + \sum_{m\neq 0, m\neq n} m(iA_m)(n-m)A_{n-m}h(n,m), \tag{23}$$

where in order to keep the results in a compact form, we introduced the coefficients

$$\alpha(n) = \frac{|n|(|n|-1)}{(2|n|-1)}, \tag{24}$$

$$\beta(n) = \frac{n^2}{(2|n|-1)}, \tag{25}$$

$$h(n,m) = \frac{1}{2|n|-1}\left((1-|n-m|)\mathrm{sgn}(m) - 2(n-m) + \frac{n}{2}\{1-\mathrm{sgn}[m(n-m)]\}\right), \tag{26}$$

and

$$k(n,m) = \frac{1}{n}\left[\mathrm{sgn}(m) - (|n|-1)h(n,m)\right]. \tag{27}$$

Note that $\mathrm{sgn}(n) = 1$ if $n > 0$ and $\mathrm{sgn}(n) = -1$ if $n < 0$.

Using Eqs. (21)–(23), which are consistent with the solvability condition and Darcy's law (10), we can derive the general expression of the vector potential Fourier coefficients in terms of the perturbation amplitudes. To fulfill this goal, consider the generalized pressure jump condition at the interface can be written as [2]

$$P|_{\mathcal{R}} = -\Gamma\kappa_{\parallel}|_{\mathcal{R}}, \tag{28}$$

where

$$\Gamma = \frac{b^2\pi\gamma}{6\eta R_f Q} \tag{29}$$

is a surface tension parameter, and $\kappa_{\parallel}$ is the curvature in the direction parallel to the plates. By expanding Eq. (28) up to the second order in ζ and up to first order in δ we find the coefficient of the vector potential corresponding to the nth evolution mode, $A_n^{(k)}$, in terms of the kth order in ζ ($k = 1,2$)

$$iA_n^{(1)}(t) = \left[\frac{R}{n}\dot{\zeta}_n + \frac{1}{nR}\zeta_n\right][1-\delta R\alpha(n)],$$

$$iA_n^{(2)}(t) = \frac{1}{R}\sum_{m\neq n,0}\left\{\frac{1}{2R\,\mathrm{sgn}(n)} + \frac{\Gamma}{\mathrm{sgn}(n)R^2}\left[2m^2 + \frac{m(n-m)}{2} - 1\right] + \delta u(n,m)\right\}\zeta_m\zeta_{n-m} + \sum_{m\neq n,0}[1+\delta R v(n,m)] \times \dot{\zeta}_m\zeta_{n-m} + \delta R^3\sum_{m\neq n,0}\frac{k(n,m)}{\mathrm{sgn}(n)}\dot{\zeta}_m\dot{\zeta}_{n-m} + \delta R\sum_{m\neq n,0}\frac{k(n,m)}{\mathrm{sgn}(n)}\zeta_m\dot{\zeta}_{n-m}, \tag{30}$$

where the overdot denotes total time derivative, and the coefficients

$$u(n,m) = \frac{1}{\mathrm{sgn}(n)}\left(k(n,m) + \left(1-\frac{1}{|m|}\right)\beta(m) - \alpha(m) - \beta(n)\left\{\frac{1}{2} + \frac{\Gamma}{R}\left[2m^2 + \frac{m(n-m)}{2} - 1\right]\right\}\right), \tag{31}$$

$$v(n,m) = \frac{1}{\mathrm{sgn}(n)}\left[k(n,m) - \beta(n) + \left(1-\frac{1}{|m|}\right)\beta(m) - \alpha(m)\right]. \tag{32}$$

To conclude our derivation we need one more step. The vector potential coefficients can be introduced into the kinematic boundary condition [2,14]

$$\frac{\partial\mathcal{R}}{\partial t} = \left[\frac{1}{r}\frac{\partial\mathcal{R}}{\partial\theta}(-v_\theta) + v_r\right]_{|_{\mathcal{R}}}, \tag{33}$$

which states that the normal components of each fluid's velocity at the interface equals the velocity of the interface itself. By using Eq. (33) plus Darcy's law (10) and Eq. (30) one can finally find the equation of motion for perturbation amplitudes ζ_n. We present the evolution of the perturbation amplitudes in terms of δ and the kth order in the perturbation amplitude ζ

$$\dot{\zeta}_n = \dot{\zeta}_n^{(1)} + \dot{\zeta}_n^{(2)}, \tag{34}$$

where

$$\dot{\zeta}_n^{(1)} = \lambda(n)\zeta_n, \tag{35}$$

$$\lambda(n) = \frac{1}{R^2}(|n|-1) - \frac{\Gamma}{R^3}|n|(n^2-1) + \delta\frac{|n|}{2|n|-1}\left[\frac{|n|-1}{R} + \frac{\Gamma}{R^2}|n|(n^2-1)\right] \tag{36}$$

is the linear growth rate, and

$$\dot{\zeta}_n^{(2)} = \sum_{m\neq n,0}[F_N(n,m) + \delta F_{NN}(n,m)]\zeta_m\zeta_{n-m} + \sum_{m\neq n,0}[G_N(n,m) + \delta G_{NN}(n,m)]\dot{\zeta}_m\zeta_{n-m} + \delta\sum_{m\neq n,0}H_{NN}(n,m)\zeta_m\dot{\zeta}_{n-m} + \delta\sum_{m\neq n,0}J_{NN}(n,m)\dot{\zeta}_m\dot{\zeta}_{n-m}. \tag{37}$$

In Eq. (37) the coefficients $F_N, F_{NN}, G_N, G_{NN}, H_{NN}$, and J_{NN} represent the second-order Newtonian (N) and

non-Newtonian (NN) terms. Their detailed functional form are presented in Appendix A. These second-order coefficients present special reflection symmetries $\mathcal{C}(n,-m)=\mathcal{C}(-n,m)$, and $\mathcal{C}(-n,-m)=\mathcal{C}(n,m)$, where $\mathcal{C}=F_N,F_{NN},G_N,G_{NN}$, H_{NN}, and J_{NN}.

Equation (34) is the mode-coupling equation of the Saffman-Taylor problem with yield stress fluids in radial geometry. It gives us the time evolution of the perturbation amplitudes ζ_n, accurate to second order, in the weak yield stress limit. Notice that Eq. (34) is conveniently written in terms of two dimensionless parameters: δ [Eq. (9)] and Γ [Eq. (29)]. The generalized Darcy law (10) and the equation of motion (34) constitute central results of this work.

IV. DISCUSSION

We proceed by using our mode-coupling approach to investigate the interface evolution at first and second order in ζ. To simplify our discussion it is convenient to rewrite the net perturbation (12) in terms of cosine and sine modes

$$\zeta(\theta,t)=\zeta_0+\sum_{n=1}^{\infty}[a_n(t)\cos(n\theta)+b_n(t)\sin(n\theta)], \tag{38}$$

where $a_n=\zeta_n+\zeta_{-n}$ and $b_n=i(\zeta_n-\zeta_{-n})$ are real-valued. Without loss of generality, for the remainder of this work, we choose the phase of the fundamental mode so that $a_n>0$ and $b_n=0$. Henceforth, we study the development of interfacial instabilities, and to examine how the yield stress parameter δ and the effective surface tension Γ affect pattern morphology. It should be noted that the theoretical results presented in the following sections utilize dimensionless quantities which are extracted from the realistic physical parameters used in the experiments of Refs. [14–16] and [43,44].

A. First order: Linear regime

Before analyzing the weakly nonlinear regime, and try to understand how nonlinearity affects the morphology of the emerging patterns, we briefly discuss some useful information which can be extracted from the linear growth rate (36). The wave number of maximum growth [obtained by setting $d\lambda(n)/dn=0$] for a Newtonian fluid ($\delta=0$) can be easily calculated from Eq. (36), yielding

$$n_{\max}^{N}=\sqrt{\frac{1}{3}\left(1+\frac{R}{\Gamma}\right)}. \tag{39}$$

From Eq. (36), one can obtain an explicit solution for the wave number $n_{\max}$ with maximal growth rate for a yield stress fluid ($\delta\neq 0$). Although this expression is rather complex, in the limit $\Gamma\ll 1$ and $n_{\max}^{N}\gg 1$ it simplifies to (see Appendix B)

$$n_{\max}\approx n_{\max}^{N}\left(1+\frac{\delta R}{4}\right). \tag{40}$$

It is worth noting that a similar kind of approximation has been performed in Ref. [35], leading to their Eq. (62). We stress that this limit (very small Γ) is consistent with experimental data of Refs. [14–16] and [43,44] which imply in Γ of the order of 10^{-3}. We have also verified that the critical wave number [obtained by setting $\lambda(n)=0$], that is the maximum wave number for which the growth rate is still positive, is shifted towards higher wave numbers as the yield stress parameter δ is increased. From these findings it is evident that yield stress effects tend to destabilize the interface in the weak yield stress regime.

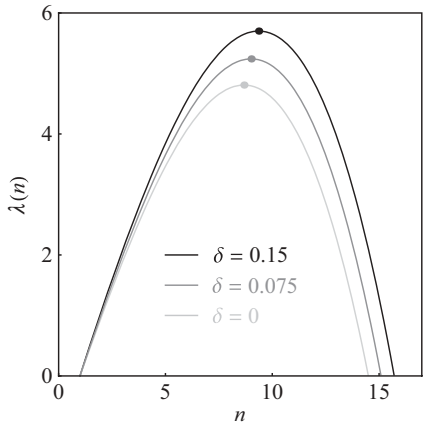

FIG. 2. Linear growth rate $\lambda(n)$ as a function of mode n, for three values of δ, surface tension parameter $\Gamma=4.45\times10^{-3}$, and $t=t_f=0.495$. To better guide the eye the maxima of the curves are explicitly indicated by small dots.

Further insight on the linear behavior can be obtained from Fig. 2, which plots $\lambda(n)$ as a function of mode number n for three different values of the yield stress parameter δ (0, 0.075, and 0.15), and $\Gamma=4.45\times10^{-3}$. By examining Fig. 2, we notice that by increasing δ one observes an increased growth rate of the fastest growing mode $n_{\max}$, so that it is shifted towards larger wave number values. Since $n_{\max}$ is related to the typical number of fingers formed at the onset of the instability, this means that higher δ would induce the formation of patterns tending to present an increased number of fingered structures. It is also clear that the action of yield stress widens the band of unstable modes. These linear stability results indicate that interfacial instabilities involving multifingered structures presenting finger tip splitting and side branching would be plausible candidates to arise due to the action of yield stress effects.

B. Second order: Weakly nonlinear regime

Now the mode-coupling equation (34) is utilized in its entirety to study the onset of pattern formation through the coupling of a small number of modes. Specifically, we will be interested in examining the action of the yield stress parameter δ on the mechanisms of finger tip splitting and side branching.

1. Tip-splitting mechanism

Within the scope of our mode-coupling theory, finger tip splitting and finger tip narrowing are related to the influence of a fundamental mode n on the growth of its harmonic $2n$ [18,36]. For consistent second-order expressions, we replace the time derivative terms $\dot{a}_n$ and $\dot{b}_n$ by $\lambda(n)a_n$ and $\lambda(n)b_n$, respectively. Under these circumstances the equation of motion for the cosine mode $2n$ is

$$\dot{a}_{2n}=\lambda(2n)a_{2n}+\tfrac{1}{2}T(2n,n)a_n^2, \tag{41}$$

where the tip-splitting function is given by

$$T(n,m) = F_N(n,m) + \lambda(m)G_N(n,m) + \delta[F_{NN}(n,m) + \lambda(m)G_{NN}(n,m) + \lambda(n-m)H_{NN}(n,m) + \lambda(m)\lambda(n-m)J_{NN}(n,m)]. \quad (42)$$

Equation (41) shows that the presence of the fundamental mode n forces growth of the harmonic mode $2n$. The function $T(2n,n)$ acts like a driving force and its sign dictates if finger tip splitting is favored or not by the dynamics. If $T(2n,n) < 0$, a_{2n} is driven negative, precisely the sign that leads to finger tip widening and finger tip splitting. If $T(2n,n) > 0$ growth of $a_{2n} > 0$ would be favored, leading to outwards-pointing finger tip narrowing.

Figure 3 plots the behavior of $T(2n,n)$ as a function of δ, for two different values of the surface tension parameter Γ. To simplify our analysis we consider the onset of growth of mode $2n$ [using the condition $\lambda(2n) = 0$] in the Newtonian limit $\delta = 0$, where we know $T(2n,n)$ is negative [18]. By inspecting Fig. 3 we see that, regardless of the value of Γ, $T(2n,n)$ becomes more negative as δ increases, driving a_{2n} negative [see Eq. (41)]. Considering the presence of only modes n and $2n$ this indicates an enhanced tendency of the fingers to get wider, and possibly split. These second-order results are consistent with the first-order predictions described in Sec. IV A, which associated larger δ with finger proliferation.

It is important to notice that, although Fig. 3 indicates an increasing tendency to observe tip splitting for larger values of δ and lower values of Γ, this is not sufficient to guarantee that finger tip splitting will be the dominant morphological feature. It is necessary to analyze the interplay between the tip splitting and other relevant nonlinear phenomena such as side-branching in order to determine the ultimate shape of the evolving pattern. In the following section we investigate the role of the side-branching mechanism in our system, and analyze which effect prevails for each set of dimensionless parameters.

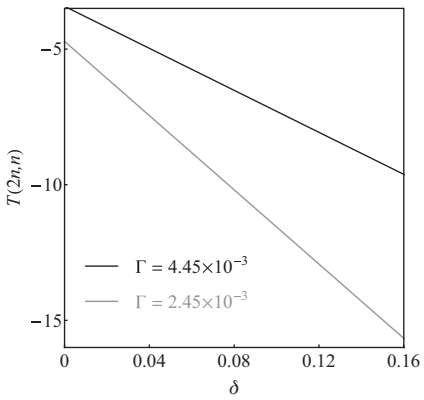

FIG. 3. Tip-splitting function $T(2n,n)$ plotted against the yield stress parameter δ, for two values of the surface tension parameter Γ: 4.45×10^{-3}, and 2.45×10^{-3}. Here $t = t_f = 0.495$. Note that the qualitative behavior of $T(2n,n)$ is basically the same for the two values of Γ. As expected, for a given δ, smaller Γ leads to enhanced tendency towards finger tip widening and splitting.

2. Side branching mechanism

Another relevant non-Newtonian effect that can be studied at second order refers to the side-branching phenomenon [36]. In the realm of a mode-coupling theory, side branching requires the presence of mode $3n$. If the harmonic mode amplitude a_{3n} is positive and sufficiently large, it can produce interfacial lobes branching out sidewards which we interpret as side branching.

As commented at the introduction of this work, an experimental study of radial Hele-Shaw flow with yield stress fluids (in the regime where viscous effects are prevalent over yield stress), detected the development of patterns exhibiting occasional tip splitting and dominant side branching [44]. Taking these experimental facts into consideration we analyze the interplay of three modes: n, $2n$, and $3n$. More precisely, we examine the influence of the fundamental mode n, and its harmonic $2n$, on the growth of mode $3n$. The equation of motion for the cosine $3n$ mode is

$$\dot{a}_{3n} = \lambda(3n)a_{3n} + \tfrac{1}{2}S(3n)a_n a_{2n}, \quad (43)$$

where the side-branching function $S(3n) = [T(3n,n) + T(3n,2n)]$ can be easily obtained from Eq. (42). By analyzing Eq. (43) we observe that mode $3n$ can be spontaneously generated due to the driving term proportional to $a_n a_{2n}$, such that it enters through the dynamics even when it is missing from the initial conditions. The existence and phase of mode $3n$ depends on the interplay of the modes n and $2n$. Side branching would be favored if $a_{3n} > 0$.

To study the growth of mode $3n$, in Fig. 4 we plot the function $S(3n)$ as the yield stress parameter is varied. Here, we consider the onset of growth of mode $3n$ [i.e. obeying the condition $\lambda(3n) = 0$] in the Newtonian limit $\delta = 0$. From Fig. 4 one can verify that $S(3n)$ is indeed negative for all values of δ. As shown in Sec. IV B1, starting with a fundamental mode a_n, the harmonic mode a_{2n} is driven negative. Hence the product $S(3n)a_n a_{2n}$ in Eq. (43) is positive, driving $a_{3n} > 0$, exactly the sign that favors side branching. Of course, whether side branching actually occurs depends on the magnitude of a_{3n}.

It is worth pointing out that there exists a subtle interconnection between modes $3n$ and $2n$, described by the evolution

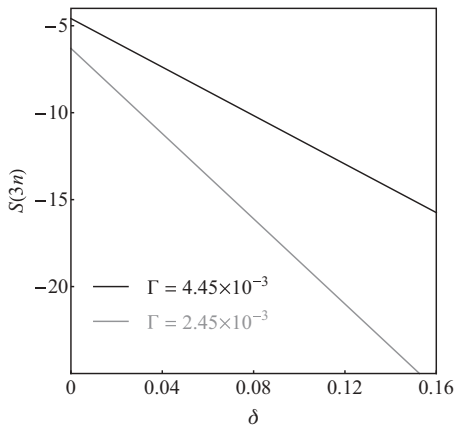

FIG. 4. Behavior of the side-branching function $S(3n)$ as the yield stress parameter δ is increased, for two values of the surface tension parameter Γ: 4.45×10^{-3} and 2.45×10^{-3}. Here $t = t_f = 0.495$.

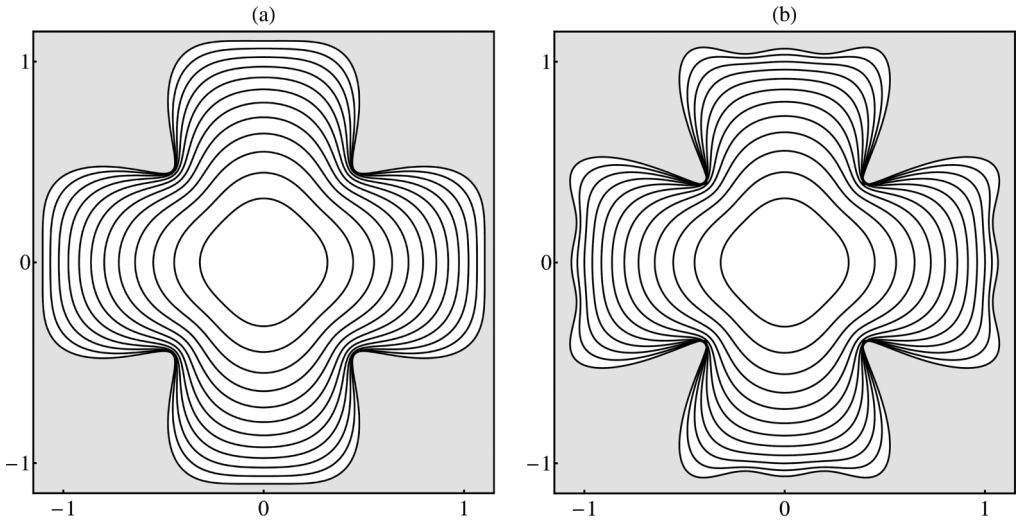

FIG. 5. Snapshots of the evolving interface, plotted at equal time intervals for the interaction of three cosine modes $n = 4$, $2n = 8$, and $3n = 12$ when (a) $\delta = 0$, and (b) $\delta = 0.15$. Here $\Gamma = 4.45 \times 10^{-3}$, $t = t_f = 0.495$, and $R_0 = 0.1$. In (a) fingers widen and tip splitting is imminent, while in (b) the rising of three-lobed finger shapes indicate that side branching is favored.

equation (43), and a similar expression for the growth of mode $2n$,

$$\dot{a}_{2n} = \lambda(2n)a_{2n} + \tfrac{1}{2}\left[T(2n,n)a_n^2 + S_{2n}a_n a_{3n}\right], \qquad (44)$$

where $S_{2n} = [T(2n,-n) + T(2n,3n)]$ is positive, but decreases in magnitude as δ is increased. Hence, when $\delta = 0$ side branching via a positive a_{3n} will tend to drive a_{2n} less negative, diminishing the intensity of tip splitting but also, as a by-product, reducing a the growth rate of a_{3n} itself. Fortunately, these effects become less important when $\delta > 0$, so that side branching could still be detected by properly tuning δ and Γ.

The role of the yield stress parameter in determining the side-branching behavior is illustrated in Fig. 5, which depicts the time evolution of the interface, plotted at equal time intervals, considering the interaction of three representative cosine modes: a fundamental $n = 4$ and its harmonics $2n = 8$, and $3n = 12$. The final time is $t = 0.495$, $R_0 = 0.1$, and $\Gamma = 4.45 \times 10^{-3}$. The initial amplitudes at $t = 0$ are $a_n = R_0/(32.5)$, $a_{2n} = 0$, and $a_{3n} = 0$, so that modes $2n$ and $3n$ are both initially absent.

In Fig. 5(a), when yield stress effects are absent ($\delta = 0$), we see a nearly circular initial interface evolving to a four-fingered structure. Finger broadening can be observed and, at later times, the finger tips become increasingly flat, showing a tendency to bifurcate. The development of broad fingers in Fig. 5(a) results from nonlinear effects, as predicted by Eq. (41), when the mode $2n$ is driven negative. Notice that there is no sign of the presence of a mode $3n$ in Fig. 5(a), indicating that side branching would not be favored when $\delta = 0$.

A different scenario is observed in Fig. 5(b), where the yield stress parameter is nonzero ($\delta = 0.15$). Contrary to what is shown in Fig. 5(a), in Fig. 5(b) we see the development of an initially fourfold structure which evolves towards a 12-fold fingered morphology, clearly showing the presence and growth of a sizable amplitude $a_{3n} > 0$. This indicates that the presence of a nonzero, sufficiently large yield stress parameter does favor side-branching formation at second order. Therefore, our weakly nonlinear results predict enhanced side-branching behavior when the role of yield stress is taken into account.

In order to reinforce the conclusions reached from Fig. 5, in Fig. 6 we compare the time evolution of the cosine perturbation amplitudes of modes n, $2n$, and $3n$ when yield stress effects are neglected (dashed curves) and taken into account (solid curves). All initial conditions and physical parameters are identical to the ones utilized in Fig. 5. It is clear that as a result of the weakly nonlinear coupling we find the enhanced growth of modes $2n$ (with $a_{2n} < 0$) and $3n$ (with $a_{3n} > 0$), and a diminished growth of the fundamental mode n. This provides supplementary information supporting the effectiveness of the side-branching formation mechanism at the onset of nonlinearity.

It is worth noting that, although in Fig. 6 a_{2n} is more negative for the yield stress case in comparison to the Newtonian one, this does not necessarily imply that tip splitting will be the prevalent morphological feature of the emergent

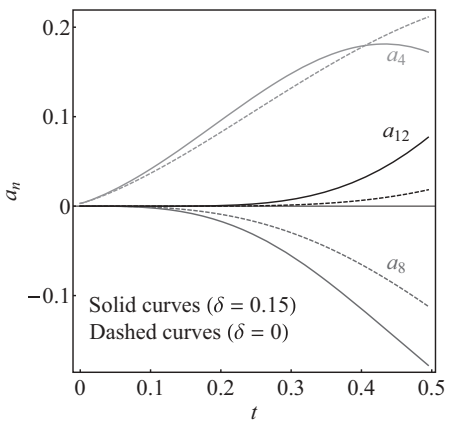

FIG. 6. Time evolution of the cosine perturbation amplitudes of modes $n = 4$, $2n = 8$, and $3n = 12$, for $\delta = 0$ (dashed curves), and $\delta = 0.15$ (solid curves). These are the amplitudes related to the patterns depicted in Fig. 5.

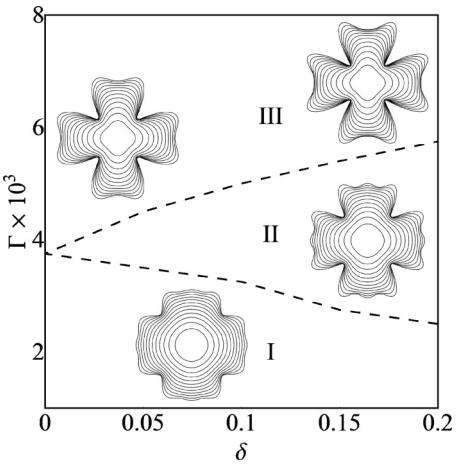

FIG. 7. Morphological phase diagram in the parameter space (δ, Γ). The dashed lines delimitate the boundary between different morphological regions (I, II, and III).

pattern. As a matter of fact, the positive amplitude of a_{3n} is also increased due to the effect of the yield stress when compared to the $\delta = 0$ situation. Consequently, side branching is also favored and eventually overcomes the tip-splitting tendency. Therefore, we find necessary to plot the interface with all three modes (n,$2n$,$3n$) put together in order to determine the prevailing mechanism at the weakly nonlinear regime. As it is further discussed, we proceed by inspecting our parameter space in Fig. 7 to unveil the final predominant morphology for each set of parameters.

We conclude this section by briefly presenting a morphological "phase diagram" for the onset of pattern formation in our radial Hele-Shaw system with a yield stress fluid. Figure 7 shows typical emerging patterns by considering the parameter space (δ, Γ). Since the parameters δ [Eq. (9)] and Γ [Eq. (29)] depend on the final unperturbed radius R_f, the representative patterns shown in the insets of Fig. 7 are plotted in such a way that R_f and R_0 are kept fixed, while the initial perturbation amplitudes are chosen in order to allow better visualization of the nonlinear effects. In other words, we choose the adequate perturbation amplitudes such that at $R = R_f$ the weakly nonlinear evolution reaches its limit of validity (interfaces plotted at different times do not intercept [53]). For this reason the initial conditions of the four insets of Fig. 7 are not exactly the same, presenting small differences in their innermost interfacial contours.

In the phase diagram depicted in Fig. 7 we can identity three different regions: for lower values of Γ and nonzero δ (region I) we verify that tip splitting is unfavored for a nonNewtonian yield stress fluid, so that the resulting patterns present a small bump in the middle of each evolving finger, indicating preferred side-branching behavior. On the other hand, for higher values Γ (region III) finger tip splitting arises without any evident manifestation of side branching, generating petal-like patterns which are similar to the ones obtained in the purely Newtonian problem when δ is small. It is also clear that stronger splitting results when δ is increased, leading to shapes showing fingers with increased spreading. Finally, for intermediate values of Γ (region II) we have the delicate interplay between modes $2n$ and $3n$ mentioned earlier [Eqs. (43) and (44)], leading to a competition between the two participating mechanisms, which ends up forming three-lobed, side-branched structures. The phase diagram contemplates the possibility of existence of tip-splitting events (region III), plus the prevalence of side-branching phenomena (regions I and II), being generally consistent with available experimental results [43,44].

V. CONCLUDING REMARKS

In this work we have considered a modified version of the Saffman-Taylor viscous fingering problem in radial Hele-Shaw geometry. In contrast to the conventional purely Newtonian situation, we have examined the case in which a fluid of negligible viscosity displaces a viscous yield stress fluid. Motivated by existing experiments [43,44] we have focused on the regime in which viscous effects prevail over yield stress. These experiments revealed the rising of ramified structures, presenting some tip-splitting events, but the predominance of side-branching phenomena.

In order to get some analytical insight into the onset of pattern formation we have derived two main theoretical results: First, using the lubrication approximation we deduced a Darcy-like law for the gap-averaged problem. Then by employing a perturbative weakly nonlinear approach we have found the mode-coupling differential equation which governs the time evolution of the interface at lowest nonlinear order. In this framework, we have shown that consideration of the coupling between a small number of modes allows one to predict and detect the occurrence of both tip splitting and side branching.

Finger widening and splitting occur through the favored growth of the harmonic mode $2n$, while side branching develops through the enhanced growth of mode $3n$. Nonlinear mode-coupling enhances the growth of these specific perturbations with appropriate relative phases. Last, we provided a morphological phase diagram that shows the flow and fluid parameters required to develop either tip splitting or side branching. In conclusion, we have developed a relatively simple analytical model which is able to capture the most salient features of this interesting and complex pattern formation problem.

ACKNOWLEDGMENTS

We thank CNPq (Brazilian Research Council) for financial support through the program "Instituto Nacional de Ciência e Tecnologia de Fluidos Complexos (INCT-FCx)."

APPENDIX A: EXPRESSIONS FOR THE SECOND-ORDER TERMS

This Appendix presents the expressions for the second-order Newtonian (N) and non-Newtonian (NN) mode-coupling coefficients which appear in Eq. (37):

$$F_N(n,m) = \frac{|n|}{R^3}\left[\frac{1}{2} - \mathrm{sgn}(nm) - \frac{\Gamma}{R}\left(1 - \frac{nm}{2} - \frac{3m^2}{2}\right)\right], \tag{A1}$$

$$F_{NN}(n,m) = \frac{1}{R^2}\left\{\left(2-\frac{n}{m}\right)\alpha(m) + |n|\left[\frac{1}{2}-\frac{\Gamma}{R}\left(1-\frac{nm}{2}-\frac{3m^2}{2}\right)\right][\alpha(n)-\beta(n)] + |n|\left[\left(1-\frac{1}{|m|}\right)\beta(m)-\alpha(m)\right]+f(n,m)\right\}, \tag{A2}$$

$$G_N(n,m) = \frac{|n|}{R}\left[1-\mathrm{sgn}(nm)-\frac{1}{|n|}\right], \tag{A3}$$

$$G_{NN}(n,m) = \left(2-\frac{n}{m}\right)\alpha(m) + |n|\left[\alpha(n)-\beta(n)+\left(1-\frac{1}{|m|}\right)\beta(m)-\alpha(m)\right] + f(n,m), \tag{A4}$$

$$H_{NN}(n,m) = f(n,m), \tag{A5}$$

and

$$J_{NN}(n,m) = R^2 f(n,m), \tag{A6}$$

where

$$f(n,m) = nh(n,m) + |n|k(n,m). \tag{A7}$$

APPENDIX B: DERIVATION OF EQ. (40)

This appendix describes the main steps of the derivation of Eq. (40). By using Eq. (36) and setting $[d\lambda(n)/dn]_{n=n_{\max}} = 0$ for the situation in which $\delta \neq 0$, we obtain a complicated equation for $n_{\max}$

$$\frac{1}{R^2}-\frac{\Gamma}{R^3}\left(3n_{\max}^2-1\right)+\delta\left\{\frac{\left(2n_{\max}^2-2n_{\max}+1\right)}{(2n_{\max}-1)^2}\left(\frac{1}{R}\right) + \left(\frac{\Gamma}{R^2}\right)\frac{2n_{\max}\left(3n_{\max}^3-2n_{\max}^2-n_{\max}+1\right)}{(2n_{\max}-1)^2}\right\} = 0. \tag{B1}$$

By considering the limit $\Gamma \ll 1$, so that the product $\delta\Gamma$ is negligibly small, Eq. (B1) can be rewritten in a much simpler form

$$\frac{\Gamma}{R}\left(3n_{\max}^2-1\right) = 1+\delta R\left\{\frac{2n_{\max}^2-2n_{\max}+1}{(2n_{\max}-1)^2}\right\}. \tag{B2}$$

Recalling that we only consider contributions up to first order in δ, notice that on the right hand side of Eq. (B2) we can replace $n_{\max}$ by $n_{\max}^N$ [Eq. (39)] without loss of generality. In this context, and assuming that $(n_{\max}^N)^2 \gg n_{\max}^N \gg 1$, we may approximate $(2n_{\max}^2-2n_{\max}+1)/(2n_{\max}-1)^2 \approx 1/2$. Thus, Eq. (B2) is simplified further, leading to

$$n_{\max} = \sqrt{\frac{R}{3\Gamma}}\left(1+\frac{\Gamma}{R}+\frac{\delta R}{2}\right)^{1/2}. \tag{B3}$$

By utilizing this equation plus Newton's generalized binomial theorem [54]

$$(x+y)^r = x^r + rx^{r-1}y + \cdots, \tag{B4}$$

where $x = 1+\Gamma/R$, $y = \delta R/2$, and $r = 1/2$ we get

$$n_{\max} = \sqrt{\frac{R}{3\Gamma}}\left[\sqrt{1+\frac{\Gamma}{R}}+\frac{\delta R}{4}\frac{1}{\sqrt{1+\frac{\Gamma}{R}}}+O(\delta^2)\right] = \sqrt{\frac{1}{3}\left(1+\frac{R}{\Gamma}\right)}+\frac{\delta R}{4}\frac{\sqrt{\frac{R}{3\Gamma}}}{\sqrt{1+\frac{\Gamma}{R}}}. \tag{B5}$$

By considering the situation $\Gamma \ll 1$, we may write $(1+R/\Gamma) \approx R/\Gamma$ and $(1+\Gamma/R) \approx 1$. Then, Eq. (B5) leads to

$$n_{\max} \approx \sqrt{\frac{1}{3}\left(1+\frac{R}{\Gamma}\right)}\left(1+\frac{\delta R}{4}\right). \tag{B6}$$

With the help of Eq. (39), this last expression readily leads to Eq. (40).

[1] P. G. Saffman and G. I. Taylor, Proc. Roy. Soc. London Ser. A **245**, 312 (1958).
[2] G. M. Homsy, Annu. Rev. Fluid Mech. **19**, 271 (1987); K. V. McCloud and J. V. Maher, Phys. Rep. **260**, 139 (1995); J. Casademunt, Chaos **14**, 809 (2004).
[3] J. V. Maher, Phys. Rev. Lett. **54**, 1498 (1985).
[4] G. Tryggvason and H. Aref, J. Fluid Mech. **136**, 1 (1983).
[5] A. J. DeGregoria and L. W. Schwartz, J. Fluid Mech. **164**, 383 (1986).
[6] E. Meiburg and G. M. Homsy, Fluids **31**, 429 (1988).
[7] C.-W. Park and G. M. Homsy, Phys. Fluid **28**, 1583 (1985).
[8] P. Tabeling, G. Zocchi, and A. Libchaber, J. Fluid Mech. **177**, 67 (1987).
[9] T. Maxworthy, J. Fluid Mech. **177**, 207 (1987).
[10] A. Arnéodo, Y. Couder, G. Grasseau, V. Hakim, and M. Rabaud, Phys. Rev. Lett. **63**, 984 (1989).
[11] J. A. Miranda and M. Widom, Int. J. Mod. Phys. B **12**, 931 (1998).
[12] J. Bataille, Rev. Inst. Fr. Pet. Ann. Combust. Liq. **23**, 1349 (1968).
[13] S. D. R. Wilson, J. Colloid Interface Sci. **51**, 532 (1975).
[14] L. Paterson, J. Fluid Mech. **113**, 513 (1981).
[15] J.-D. Chen, J. Fluid Mech. **201**, 223 (1989); Exp. Fluids **5**, 363 (1987).
[16] H. Thomé, M. Rabaud, V. Hakim, and Y. Couder, Phys. Fluids A **1**, 224 (1989).
[17] O. Praud and H. L. Swinney, Phys. Rev. E **72**, 011406 (2005).
[18] J. A. Miranda and M. Widom, Physica D **120**, 315 (1998).
[19] P. Fast and M. J. Shelley, J. Comput. Phys. **212**, 1 (2006).
[20] J. Mathiesen, I. Procaccia, H. L. Swinney, and M. Thrasher, Eur. Phys. Lett. **76**, 257 (2006).

[21] S. W. Li, J. S. Lowengrub, and P. H. Leo, J. Comput. Phys. **225**, 554 (2007).
[22] C.-Y. Chen, C.-W. Huang, H. Gadêlha, and J. A. Miranda, Phys. Rev. E **78**, 016306 (2008).
[23] S. W. Li, J. S. Lowengrub, J. Fontana, and P. Palffy-Muhoray, Phys. Rev. Lett. **102**, 174501 (2009).
[24] R. B. Bird, R. Armstrong, and O. Hassager *Dynamics of Polymeric Liquids* (Wiley, New York, 1977).
[25] A. Buka, P. Palffy-Muhoray, and Z. Racz, Phys. Rev. A **36**, 3984 (1987).
[26] H. Zhao and J. V. Maher, Phys. Rev. E **47**, 4278 (1993).
[27] J. Ignés-Mullol, H. Zhao, and J. V. Maher, Phys. Rev. E **51**, 1338 (1995).
[28] N. Kagei, D. Kanie, and M. Kawaguchi, Phys. Fluids **17**, 054103 (2005).
[29] J. E. Sader, D. Y. C. Chan, and B. D. Hughes, Phys. Rev. E **49**, 420 (1994).
[30] D. Bonn, H. Kellay, M. Ben Amar, and J. Meunier, Phys. Rev. Lett. **75**, 2132 (1995); D. Bonn, H. Kellay, M. Braunlich, M. Ben Amar, and J. Meunier, Physica A **220**, 60 (1995).
[31] L. Kondic, P. Palffy-Muhoray, and M. J. Shelley, Phys. Rev. E **54**, R4536 (1996).
[32] L. Kondic, M. J. Shelley, and P. Palffy-Muhoray, Phys. Rev. Lett. **80**, 1433 (1998).
[33] E. Corvera Poiré and M. Ben Amar, Phys. Rev. Lett. **81**, 2048 (1998).
[34] M. Ben Amar and E. Corvera Poiré, Phys. Fluids **11**, 1757 (1999).
[35] P. Fast, L. Kondic, M. J. Shelley, and P. Palffy-Muhoray, Phys. Fluids **13**, 1191 (2001).
[36] M. Constantin, M. Widom, and J. A. Miranda, Phys. Rev. E **67**, 026313 (2003).
[37] P. Fast and M. J. Shelley, J. Comput. Phys. **195**, 117 (2004).
[38] S. Nguyen, R. Folch, V. K. Verma, H. Henry, and M. Plapp, Phys. Fluids **22**, 103101 (2010).
[39] H. A. Barnes, J. Non-Newtonian Fluid Mech. **81**, 133 (1999).
[40] P. Moller, A. Fall, V. Chikkadi, D. Derks, and D. Bonn, Phil. Trans. R. Soc. A **367**, 5139 (2009).
[41] P. Coussot, J. Fluid Mech. **380**, 363 (1999).
[42] E. Lemaire, P. Levitz, G. Daccord, and H. Van Damme, Phys. Rev. Lett. **67**, 2009 (1991).
[43] A. Lindner, P. Coussot, and D. Bonn, Phys. Rev. Lett. **85**, 314 (2000).
[44] N. Maleki-Jirsaraei, A. Lindner, S. Rouhani, and D. Bonn, J. Phys.: Condens. Matter **17**, S1219 (2005).
[45] G. K. Batchelor, *An Introduction to Fluid Dynamics* (Cambridge University Press, Cambridge, 1967).
[46] G. Dai and R. B. Bird, J. Non-Newtonian Fluid Mech. **8**, 349 (1981).
[47] G. H. Covey and B. R. Stanmore, J. Non-Newtonian Fluid Mech. **8**, 249 (1981).
[48] S. A. Lira, J. A. Miranda, and R. M. Oliveira, Phys. Rev. E **81**, 046303 (2010).
[49] S. A. Lira, J. A. Miranda, and R. M. Oliveira, Phys. Rev. E **82**, 036318 (2010).
[50] G. G. Lipscomb and M. M. Denn, J. Non-Newtonian Fluid Mech. **14**, 337 (1984).
[51] S. D. R. Wilson, J. Non-Newtonian Fluid Mech. **47**, 211 (1993).
[52] J. M. Piau, J. Rheol. **40**, 711 (1996).
[53] M. J. P. Gingras and Z. Rácz, Phys. Rev. A **40**, 5960 (1989).
[54] M. Abramowitz and I. A. Stegun, *Handbook of Mathematical Functions with Formulas, Graphs, and Mathematical Tables* (Dover, New York, 1972).